Chapter 4

Nanoarchitectonics of self-assembled CB-like nanostructure by recurrent phase separation and concatenation of nanodomains in CoFeMn oxide

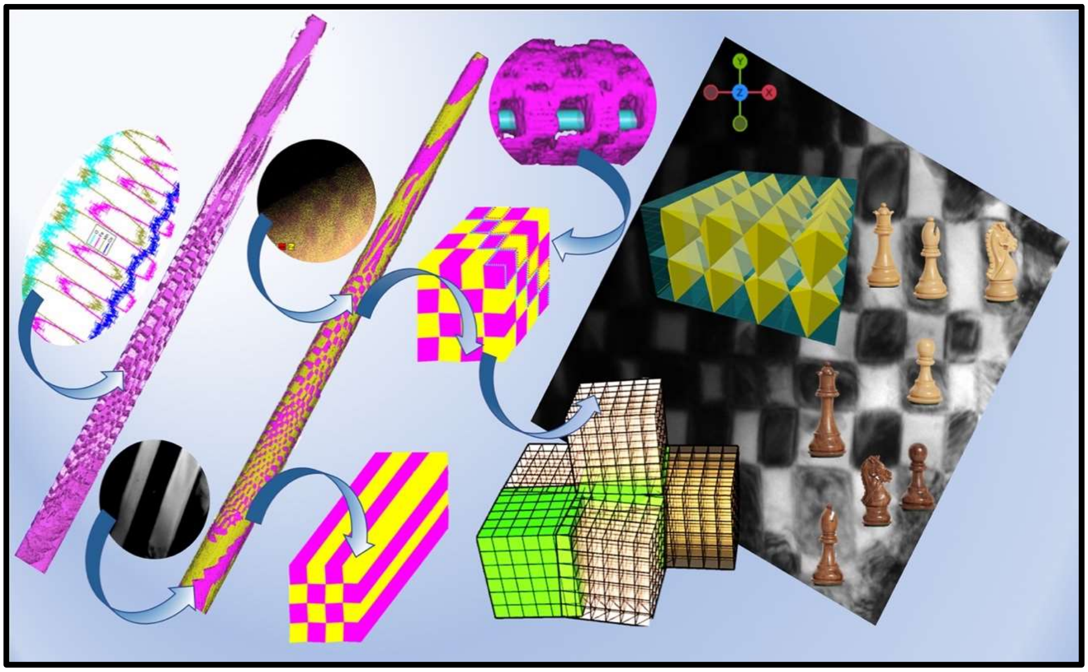

4.1 Introduction

Nanoarchitectonics of well-organized self-assembled nanostructures has been a driving force behind the continued development of nanodevices this millennium [1–5]. Nanolithography [6], template-assisted deposition [7,8], epitaxial growth [9] and order-disorder transformations [10] are all examples of possible fabrication routes. Chessboard (CB) nanostructure evolution involves the development of structurally and chemically similar, or distinct and functionally different, nanodomains in the solid state [11]. The well-defined disposition of more than one type of nanodomain in three dimensions (3D) and the directional-dependent functionalities of these nanodomains, combined with their cumulative effect overall, are together expected to lead to a periodic variation of functional properties in different crystallographic directions in 3D. This periodic variation is expected to be a key aspect for the use of such CB nanostructures in future high-density memory storage, nanoelectronic and energy devices [12–14]. CB nanostructure evolution has been reported in several metallic and ceramic systems such as AuCu-Ag [15], AuCu-Pt [15], Au-Zn II [16] and Co-Pt [10] in metallic systems; $BaTiO_3$-$CoFe_2O_4$ [17] and $Li_{3x}Nd_{2/3-x}TiO_3$ [12,13] in perovskites; and $CoFe_{2-x}Mn_xO_4$ [18], $Mg(Fe_{1-x}Mn_x)O_4$ [19] and $ZnGaMnO_4$ [9] in spinel manganates. The mechanism of CB evolution is system dependent: $Al \rightarrow Ll_2 \rightarrow L1_0 + Ll_2$ ordering occurs in the metallic systems [10,15], tilting of frustrated BO_6 octahedra occurs in the perovskites [13] and Jahn-Teller (J-T) distortions occur in the spinel manganates [9,18,19]. Irrespective of the system, computational modeling and limited experimental observation assumed that CB-like nanostructures develop in two dimensions (2D), which means in essence that these nanostructures are periodic stacking of nanorods [11,14]. However, a full understanding of the genesis and growth of such periodic nanodomains, the crystallography of the nanodomain interfaces and the chemical evolution of the nanodomains all remain active areas of research [12,13,20].

In this chapter, the author has shown through combined transmission electron microscopy (TEM) and atom probe tomography (APT) that the genesis of CB nanostructure is marked by the interpenetration of compound deformation twins accompanying the chemical segregation. Through APT this is shown to be a pseudo-spinodal decomposition leading to a sub-domain formation to enable the equilibrium state to be reached. In the initial stages of evolution, nano-cuboids/octahedra with particular interfaces and orientation relationships, and with subtle changes in structure and chemistry, form in 3D.

Subsequently, coalescence of the nano-cuboids/octahedra along specific crystallographic directions, which is most likely to be surface energy driven [14], produces the 2D CB nanostructure. This work has been undertaken with the CoFeMn mixed oxide system as the system of focus. The two different nanodomains in this system are likely to be magnetic in nature. The magnetic behavior of the final microstructure can be tailored by a suitable design of the nanodomain disposition and chemistry through careful control of the kinetics of the nanodomain formation process [18].

4.2 Materials and methods

High purity precursor powders of (CoO + Co_2O_3) Co_3O_4, Mn_2O_3 and Fe_2O_3 (>99.99% purity, Sigma Aldrich & Alfa Aesar) were mixed in a precise stoichiometric ratio to obtain a mixed oxide with a $Co_{0.6}Fe_{0.8}Mn_{1.6}O_{4+\delta}$ composition where $\delta << 1$. When calculating and weighing the oxides in stoichiometric ratios, the oxidation states of Co, Fe and Mn were taken to be +2, +3 and +3 respectively. The oxide powders were first ground by mortar and pestle, after which the mixed powder was pelletized by applying a pressure of 5 MPa through a hydraulic hand press. These green pellets were sintered in air in a covered platinum crucible at 1250 °C for 24 hours followed by quenching into iced water. The sintering process was repeated twice with an intermediate grinding of the first time sintered and quenched pellets to homogenized the chemical composition throughout the sintered pellet. In order to obtain sufficient local diffusive rearrangement of ions after quenching for second time, an extended ageing treatment was given in air atmosphere at 375 °C to some of the pellets. The pellets were characterized by X-ray diffraction (XRD) (Panalytical Empyrean High-Resolution X-ray Diffractometer) and transmission electron microscopy (TEM) (Tecnai G^2 T20 and Titan 300).

To prepare the tip for APT characterization, pre-characterized CB-samples were taken into account, and needle-shaped specimens were lifted out from vintage sites using a dual beam workstation SEM–FIB (FEI Helios Nanolab G4UX). The process is explained stepwise in references (Figure 2.4) [21,22]. To minimize the Ga+ beam damage, a low-energy milling step (5 keV) was used at the final stage of sample preparation. APT measurements were performed in pulsing laser mode (wavelength of 355 nm (UV)) on Local Electrode Atom Probe (LEAP) 5000 XR, Cameca Instruments. During the whole process, the tip temperature was maintained at 60 K. The laser pulse frequency was set to 250 kHz with 30 pJ energy. The data collection rate was 0.5% ions per field evaporation pulse. The microstructural reconstruction and data analysis were performed on the Integrated

Visualization and Analysis Software (IVAS 3.8.10) of Cameca Instruments Inc (Madison, WI, USA).

4.3 Results and discussion

4.3.1 X-ray diffraction analysis

The cubic solid solution spinel phase with a $Fd\overline{3}m$ space group ($a_c \approx 8.3$Å) forms in the $Co_{0.6}Fe_{0.8}Mn_{1.6}O_{4+\delta}$, where $\delta << 1$ after sintering at 1250 °C for 24 hours and subsequent quenching, as is evident from the X-ray diffraction pattern (Figure 4.1(b)).

After ageing the sintered and quenched sample at 375 °C for 250 hours, the sharpness of the diffraction peaks reduces (Figure 4.1(a)), and the peaks can be indexed to two spinel phases: $CoFe_2O_4$ (space group $Fd\overline{3}m$ with $a \approx 8.3$ Å) and $CoMn_2O_4$ (space group $I4_1/amd$ with $a = 5.72$ Å and $c = 9.27$ Å). For TEM observations (Figure 4.1(c-f)), it is convenient to refer to a face-centred tetragonal (FCT) unit cell description of this tetragonal phase because of its obvious and straightforward correlation with the FCC unit cell. The *I* body-centred tetragonal (BCT) unit cell is related to the FCT unit cell by a 45° rotation of x and y-axes about the z-axis and with $a_{\mathrm{FCT}} = \sqrt{2}a_{\mathrm{BCT}}$.

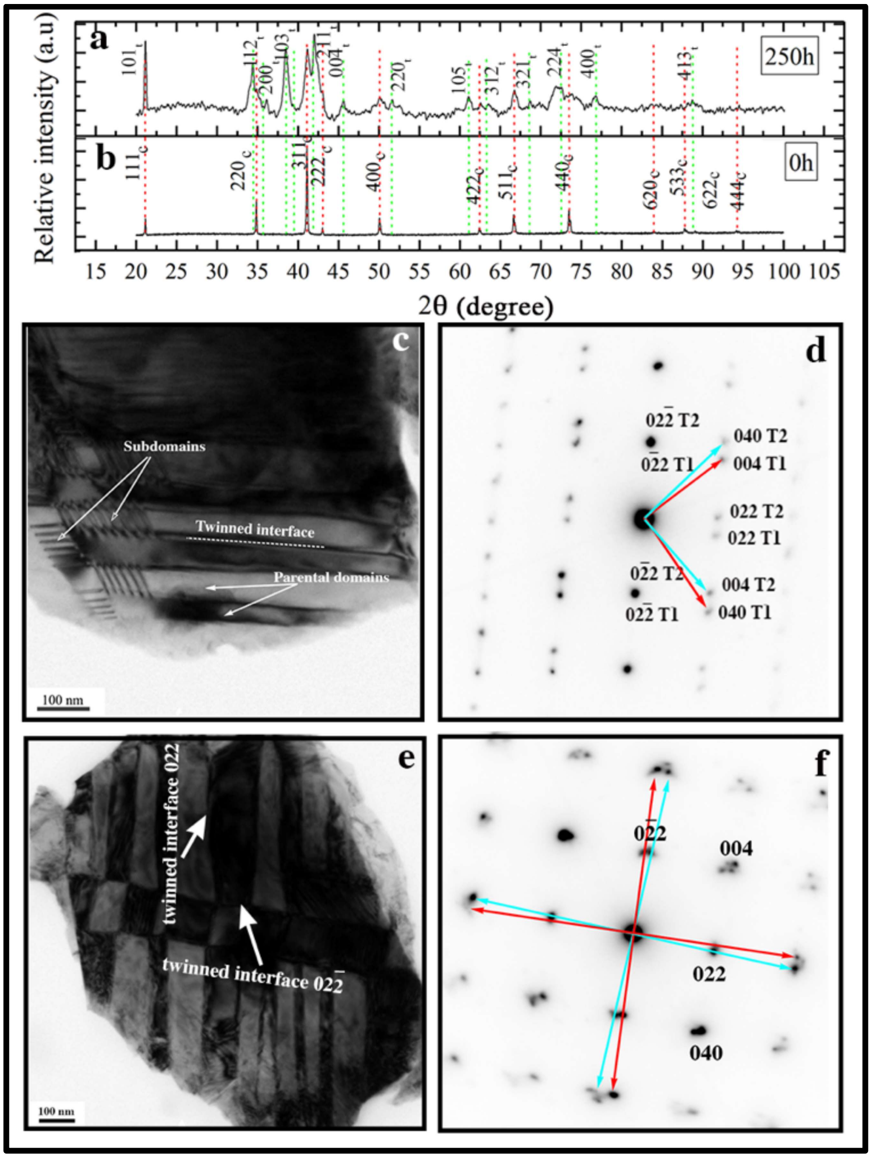

Figure 4.1: *X-ray diffraction patterns of* $Co_{0.6}Fe_{0.8}Mn_{1.6}O_{4+\delta}$*, where* $\delta << 1$ *after sintering at 1250 °C for 24 hours and subsequent quenching: (a) aged at 375 °C for 250 hours after quenching; (b) 0 hours / as-quenched. (c) Bright-field TEM image of sample aged for 250 hours and (d) the corresponding orientationally aligned diffraction pattern. (e) Bright-field TEM image of the same sample with (f) the corresponding orientationally aligned diffraction pattern showing the cross-over of the two sets of twins.*

4.3.2 Diffraction contrast imaging and Z-contrast imaging

In the TEM bright field image of the sintered, quenched and aged sample, linear contrast typical of planar faults ~70 nm wide can be observed (Figure 4.1(c)). Within these faulted regions, almost perpendicular to the fault boundaries, similar linear contrast can be observed with a ~10 nm spacing (marked as 'subdomains' in Figure 4.1(c)). These are deformation twins. Interpenetration of such twins leads to the formation of the chessboard nanostructure. The formation mechanisms, interface structure and chemistry of this nanostructure is the main focus of this chapter. The electron diffraction pattern (Figure 4.1(d)) from the faulted region (Figure 4.1(c)) taken along the [100] zone axis indicates that the linear contrast is from two adjacent twinned regions, in which $0\bar{2}2$ is the twin plane and where there are two sets of co-existing tetragonal domains twinned with respect to one another by 180° rotation about the axis normal to the plane 022. The reciprocal lattice vectors from two domains are marked by red and cyan. The twinning seen in the tetragonal phase can be described in the formal theory of deformation twinning [23] as being either defined by $K_1 = (101)$, $K_2 = (10\bar{1})$, $\eta_1 = (10\bar{1})$, $\eta_2 = [101]$, $s = (c/a) - (a/c)$ using the FCT lattice description or by $K_1 = (112)$, $K_2 = (11\bar{2})$, $\eta_1 = (11\bar{1})$, $\eta_2 = [111]$, $s = (\sqrt{2}\, c/a) - (a/\sqrt{2}\, c)$ using a BCT lattice description, where K_1, K_2, η_1, η_2 and s have their usual meanings in deformation twinning crystallography. The lattice parameters for the FCT phase calculated from the electron diffraction pattern are a_t = 8.1 Å and c_t = 8.9 Å. In comparison with the reported tetragonal $CoMn_2O_4$ phase, the 'a' parameter remains almost same, whereas there is a decrease in the 'c' parameter. This might correlate with the subtle change in chemistry of the twinned domains. This possibility has been investigated with the help of STEM-EDS and 3D APT. An almost perpendicular cross-over of faulted domains can be observed in Figure 4.1(e). The corresponding rotationally aligned diffraction pattern in Figure 4.1(f) shows the superimposition of two different twin modes. For the first set of twins, which is almost horizontal, the twin crystallography is that shown in Figure 4.1(d). For other set of twins, which are almost vertical, the twin plane is 022 and the two adjacent twin domains are related to one another by 180° rotation about an axis perpendicular to the $0\bar{2}2$ plane with respect to a FCT unit cell. The twin crystallography of the second set of twins can also be derived in a similar way to that described for Figure 4.1(d). Localized cross-over of twins (Figure 4.1(e)), produces a localized CB nanostructure. The evolution into a 'proper' CB nanostructure will be addressed in subsequent sections. Subtle splitting of the major reflections in Figure 4.1(f) as a consequence of this complex twinned crystallography is evident.

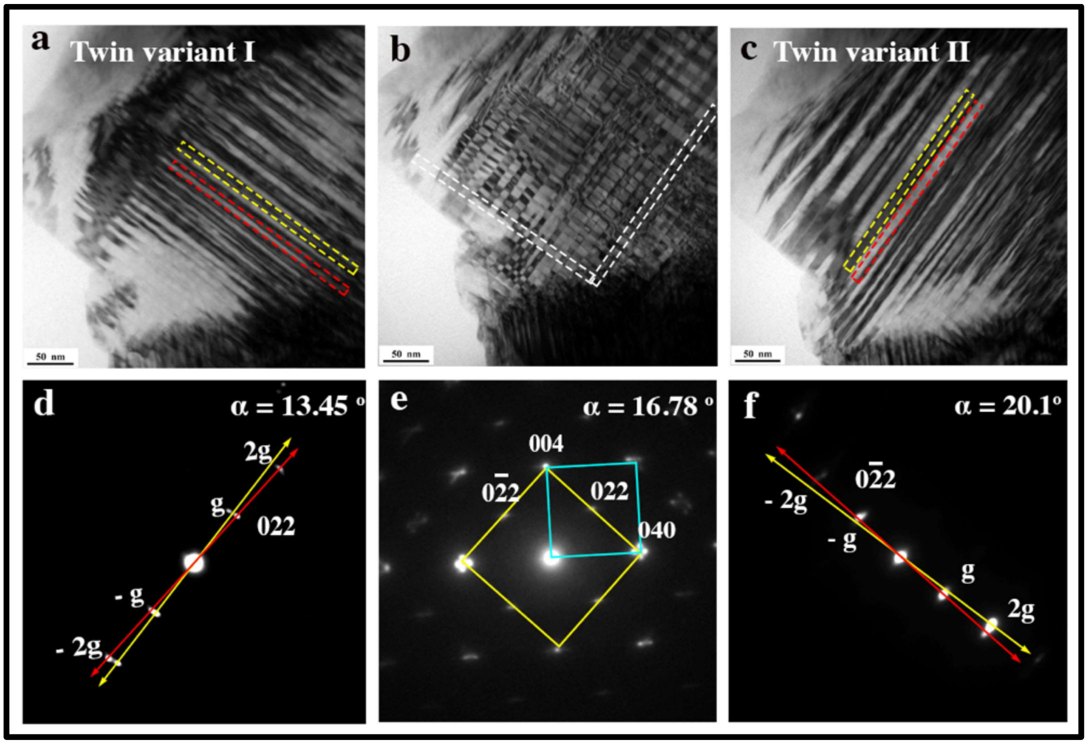

Figure 4.2(a-f): *Diffraction contrast images and corresponding diffraction patterns from the two twin variants that lead to the formation of a CB nanostructure in the* $Co_{0.6}Fe_{0.8}Mn_{1.6}O_{4+\delta}$ *where* $\delta << 1$*, which was heat treated at 1250 °C for 24 hours, followed by quenching and ageing for 25 hours at 375 °C. The cross-over of two twin variants in (b) leads to the formation of the CB nanostructure. In the corresponding [100] electron diffraction pattern in (e) both the 022 type of spots are visible. Tilting ~3° away from [100] makes twin variant I visible in (a) and in the corresponding diffraction pattern in (d) only 022 systematic spots are visible. Tilting ~3° in the other direction away from [100] makes the twin variant II visible in (c) and in the corresponding diffraction pattern in (f) only* $0\bar{2}2$ *systematic spots are visible. This confirms that the CB nanostructures initially forms by cross penetration of perpendicular twins and continuous rod like appearance is often the inability to see the other twin variant.*

The crossover of twins leading to the formation of a CB nanostructure from a different region, and their simultaneous presence at a [100] zone axis, and their alternate disappearance away from the zone axis is shown in Figure 4.2. The sample was sintered at 1250 °C for 24 hours, followed by quenching and ageing for 25 hours at 375 °C. The CB domains are ~ 8nmX8nm in size. In Figure 4.2(b) cross over of both the twin variants are visible and in the corresponding diffraction pattern (Figure 4.2(e)) both 022 and $0\bar{2}2$ reciprocal lattice vectors are active. After tilting the sample by ~3^{o} in one direction, only twin variant I is visible (Figure 4.2(a)) and in the corresponding electron diffraction pattern (Figure 4.2(d)), only 022 type of reciprocal lattice vector is active. After tilting the sample by ~3^{o} in other direction, twin variant II becomes visible (Figure 4.2(c)) and in the corresponding electron diffrcation pattern (Figure 4.2(e)), only $0\bar{2}2$ type of reciprocal lattice vector is active. This further confirms that the CB nanostructures forms by cross-penetration of perpendicular twin variants, inability to excite both the twin variants simultaneously may give rise to a rod like morphology.

4.3.3 Orientation relationship establishment

A well-developed CB nanostructure can be observed in the sintered, quenched and aged pellet, such as Figure 4.3 (a), from which the corresponding rotationally aligned diffraction pattern is shown in Figure 4.3(b). The size of the domains varies with a mean domain size of ~70 nm × 70 nm. Even though the boundaries between domains are formed from the crossover of almost perpendicular deformation twins, here, these domain boundaries do not form a network of straight lines in 2D. Instead, the boundaries show a relative twist of 5.2° in a zig-zag fashion marked by the white dotted lines in Figure 4.3(a), consistent with the diffraction pattern in Figure 4.3 (b). The 022 and $0\bar{2}2$ row of spots are split by 5.2°, indicating a relative rotation between the adjacent domains in the vertical and horizontal directions. This suggests a need to minimize the interfacial strain arising from the lattice parameter mismatch between the cubic and tetragonal components of this CB microstructure with subtle variations in chemistry in the neighboring domains, as shown in Figure 4.3 (c). A similar CB nanostructure from a different region, together with the nano-beam diffraction patterns from the domains and across the domain interfaces are given in Figure 4.4. In this figure, relative rotations between the cubic and the tetragonal domains are observed in the electron diffraction patterns.

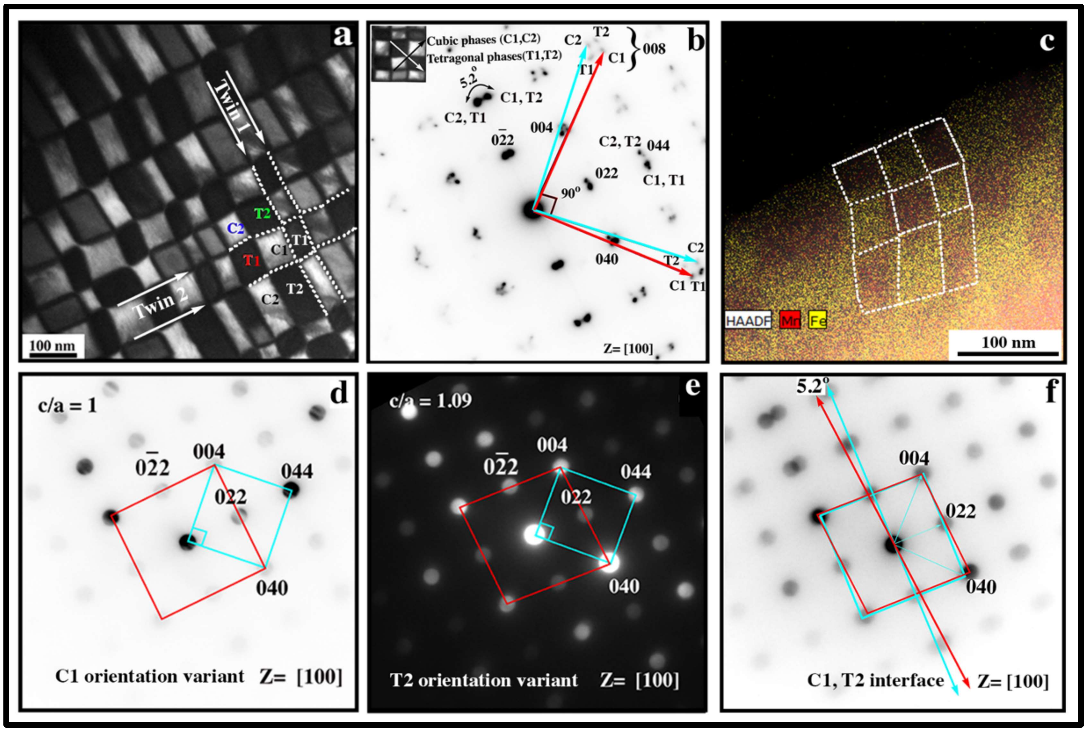

Figure 4.3: *(a) Bright-field TEM image and corresponding (b) rotationally aligned diffraction pattern from the* $Co_{0.6}Fe_{0.8}Mn_{1.6}O_{4+\delta}$*, where* $\delta << 1$ *from the sintered, quenched and aged sample. (c) STEM-EDS composition map of the same sample showing separation of Mn and Fe within the neighbouring domains. (d-f): nanobeam electron diffraction pattern from (d) the cubic domain marked as C1, and (e) the tetragonal domain marked as T2 (f) vertical interface of C2 and T2 in (a).*

The nano-beam diffraction patterns from the interfaces (Figure 4.4 (FB) and Figure 4.4 (AB)) show spot splitting confirming the relative rotation of 5.2° between adjacent domains. A similar 5.2° solid-body rotation between adjacent domains was observed in ZnMnGa oxide film leading to the formation of a CB nanostructure [9]. However, the 040 and the 004 type of reciprocal lattice spots in Figure 4.3(b) are split into four spots with uneven distribution of intensity of the spots. While the origin of the split spots in the diffraction pattern will be discussed later, the uneven distribution of intensity necessarily indicates a complex rotation between the CB domains. The nano-beam electron diffraction pattern (Figure 4.3 (d)) from the bright domain, marked as ‘C1’ in Figure 4.3(a) shows that the cubic 022 and $0\bar{2}2$ planes are its interfaces with the neighbouring domains in the horizontal and the vertical direction. Similarly, the nano-beam electron diffraction pattern

(Figure 4.3(e)) from the tetragonal dark domain, marked as ‘T1’ in Figure 4.3(a) shows similar 022 and $0\bar{2}2$ interfaces, but with a relative in-plane rotation of 5.2° between them. The symmetry of the bright domains and the dark domains are cubic and tetragonal (Figure 4.3(d, e)) with c/a ratios of 1 and 1.09 respectively.

The in-plane rotation of 5.2° between the cubic and the tetragonal domain can be reconfirmed from the nanobeam electron diffraction pattern taken from the vertical interface of C2 and T2 (Figure 4.3(f)). The cubic and the tetragonal domains appear alternatingly in the 022 type of directions and the tetragonal domains or the cubic domains form a continuous chain by sharing their corners along 004 or 040 type of directions. Subsequent to the cross-over of the deformation twins, a relative rotation between the neighbouring domains takes place in order to minimize their interfacial strain. In addition, there is a symmetry breaking transition for some of the domains leading to alternating cubic and tetragonal structures. The symmetry breaking transition may be attributed to the subtle change in chemistry in the domains as seen in Figure 4.3(c), where Fe and Mn separate out, producing Mn-rich and Fe-rich domains. Symmetry breaking transitions and subtle change in c/a ratio with the change in the ratio of (Fe+Co):Mn concentration has been reported in the literature [24]. The splitting of spots in the diffraction pattern (Figure 4.3(b)) from the CB nanostructure (Figure 4.3(a)) can be explained by the presence of four rotational variants of the cubic and the tetragonal phases, in which two are tetragonal and two are cubic in structure rotated with respect to one another by 5.2° (Figure 4.3(b) inset). The rotational variants are given in Figure 4.5(a). The cubic and the tetragonal variants are marked with four different colours. They have been named as C1, C2 for the cubic variants and T1 and T2 for the tetragonal variants.

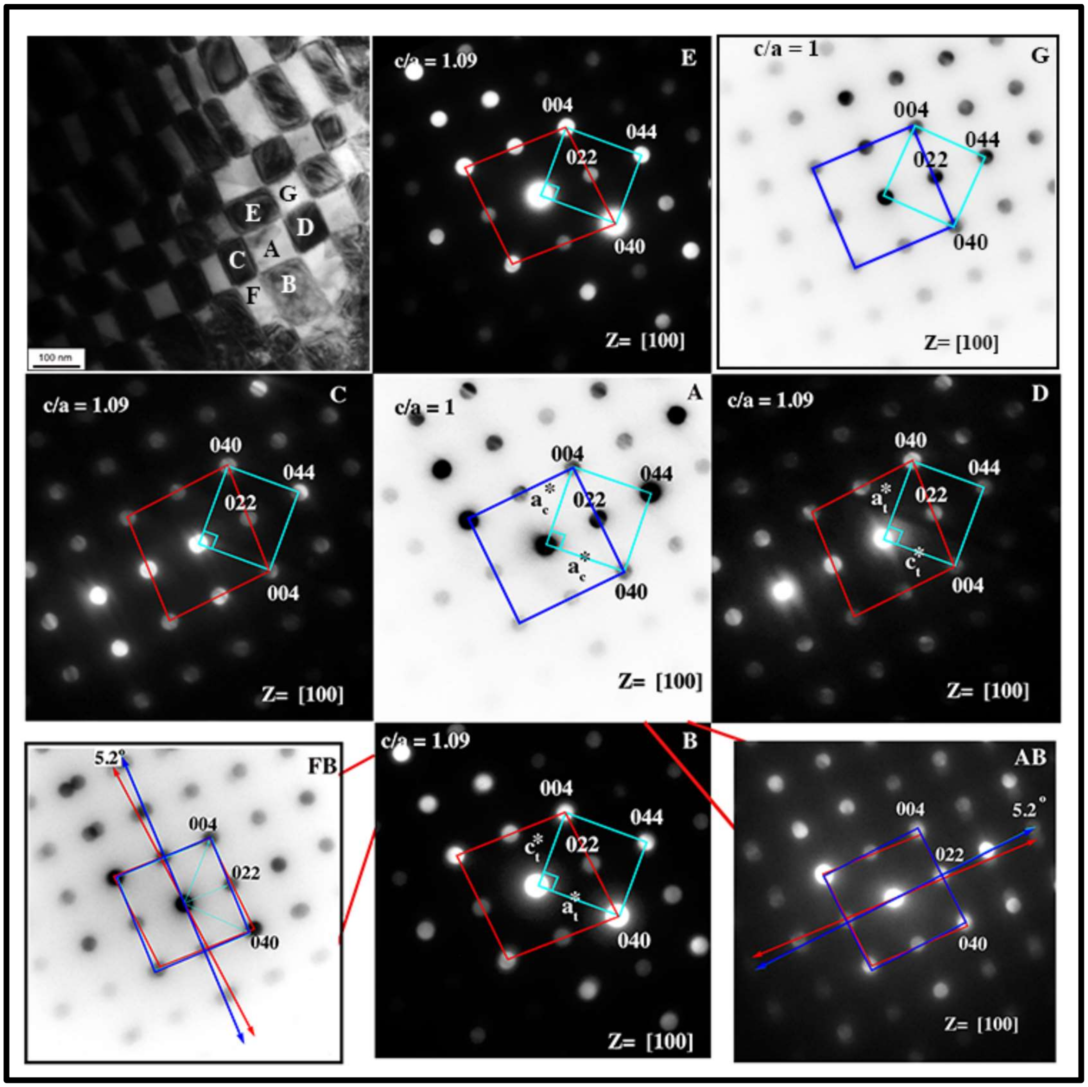

Figure 4.4: *Bright field image of the CB nanostructure and nano-beam electron diffraction patterns from the nanodomains and the interfaces in* $Co_{0.6}Fe_{0.8}Mn_{1.6}O_{4+\delta}$ *where* $\delta << 1$*. This sample was heat treated at 1250 °C for 24 hours, followed by quenching and ageing for 250 hours at 375 °C. Nanodomains are marked with 'A', 'B', 'C', 'D' 'E', 'F' and 'G' and their corresponding nano-beam diffraction patterns are given in (A-E, G). The nano-beam diffraction pattern from the interface of the domain 'A' and domain 'B' is given in 'AB' and the same from the domain 'F' and domain 'B' is given in 'FB'. Spot splitting is observed in the diffraction patterns from the interfaces indicating a relative rotation of 5.2° between the adjacent domains. Rotated cubic (C1, C2) and tetragonal (T1, T2) variants are observed from the diffraction patterns from the nanodomains and [004] of T1 is perpendicular to [004] of T2.*

The domain variants are marked with the respective colours in the CB nanodomain image in Figure 4.3(a). The [100] reciprocal lattice projection for the four domain variants are superimposed in Figure 4.5(a). In the image indexing only up to first order of reciprocal lattice reflections are given. With the black dot as the position of the 000 direct beam, it can be deduced that the four domain variants will share the 022 types of interfaces.

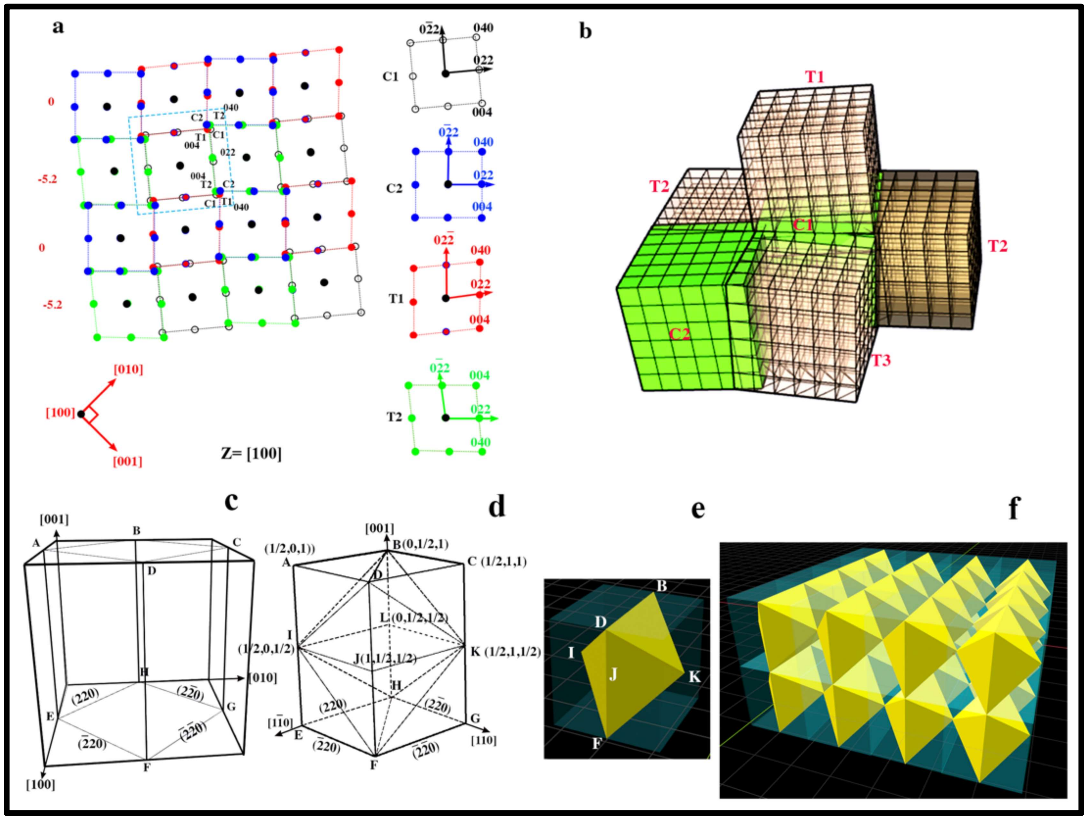

__Figure 4.5:__ (a) Composite [100] reciprocal lattice projection (up to first order reflections) of two cubic domains (C1 and C2) and two tetragonal domains (T1 and T2) leading to the splitting of reflections in the diffraction pattern from the CB nanostructure (b) 3D representation of the cubic and the tetragonal domains with in-plane and out-of-plane rotations, (c)-(e) systematic truncation of a cubic lattice that leads to the formation of octahedra with eight {220} surfaces (f) arrangement of octahedra in 3D that will appear to be a CB nanostructure from <100> directions.

As a consequence of the relative rotation, 022 types of spots are split into two and the 004 or 040 type of spots are split into four, which is observed in the electron diffraction pattern in Figure 4.3(b). It can be concluded from this observation that post cross-twinning, there is a solid body rotation between the domains (Figure 4.5(b)) in combination with the composition separation (Figure 4.3(c)), which gives rise to two rotationally variant cubic domains with same lattice parameter and two rotationally variant tetragonal domains with similar lattice parameters. Even though the evolution pathway of CB nanostructure in 2D is understood from Figures 4.2, 4.3, 4.4 and 4.5, it still remains a question as to whether such variants extend in three dimension or not.

4.3.4 Observation of subdomains, their orientation relationship and chemistry

It has been reported in the literature that the CB nanostructure develops in 2D. This has been rationalized in terms of the systematic stacking of square-like rods [11,14]. In order to examine this as a possible interpretation, the 2D CB nanostructure evident in Figure 4.3 was tilted in an attempt to obtain an image of rod-like stacking. However, while tilting, when the sample was at $[1\bar{2}\bar{2}]$ zone axis (Figure 4.6(b)), the dark-field image with the $\bar{4}\bar{2}0$ spot (Figure 4.6(a)) showed some fringe contrast within the domains, with a periodic half wavelength of ~7-10 nm. This fringe contrast could be misinterpreted as being thickness fringes. However, thickness fringes with such a small half wavelength of contrast variation is unlikely under the imaging conditions we have used. The STEM-EDS composition map (Figure 4.6(c)) from one of these domains shows a composition modulation between Fe and Mn with a similar half wavelength. Even after the formation of CB nanostructures, composition separation between Fe and Mn continues. This suggests a binary pseudo-spinodal decomposition within the domains. Another tilted version of the CB nanostructure in Figure 4.6(d) also shows rod-like features with ~70 nm width. While tilting to try and observe the rod-like morphology, split-domain like morphology within the supposed rods (Figure 4.6(e)) with half wavelength of ~10 nm could also be observed. Similar cross penetrated split domain morphology may also be seen faintly in Figure 4.6(d) (top bright rod). Though in Figure 4.6(e), only one set of parallel split domains are observed, the contrast in Figure 4.6(d) (top bright rod) indicates that similar split domains may exist in other direction also, which are not visible in Figure 4.6(e) due to specific viewing direction.

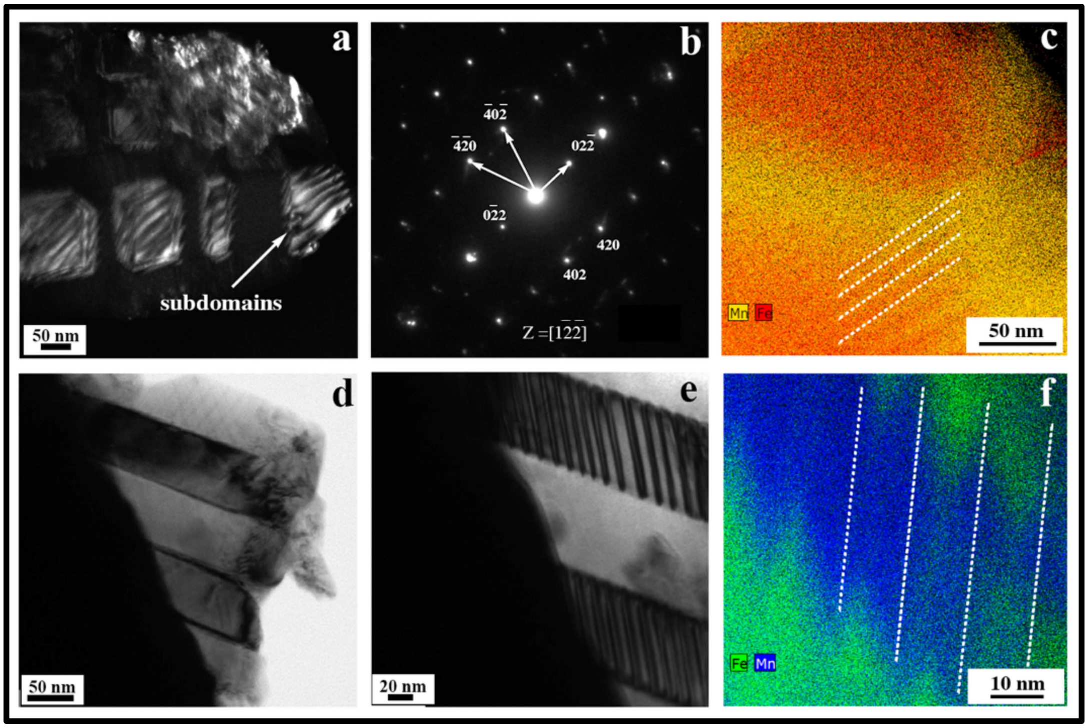

Figure 4.6: *(a) TEM dark field image of the CB domain taken from a* $\bar{4}\bar{2}0$ *reflection, (b) the corresponding diffraction pattern along Z =* $[1\bar{2}\bar{2}]$*. Subdomains within the CB domains are visible. (c) STEM-EDS composition map from the CB domain showing composition separation between Fe and Mn. This is a tilted image of the CB nanostructure. (d) TEM image showing continuous rod like appearance, tilted to (e) where it is now showing a split domain contrast. (f) STEM-EDS composition map of the image in (e) where composition separation between Fe and Mn can be observed.*

This indicates that the rods are not continuous, and that instead there is a possibility of domain formation in 3D. The STEM-EDS composition map (Figure 4.6(f)) from the split-domain like rod morphology in Figure 4.6(e) shows that there is also a composition separation between Fe and Mn with half wavelength variation of ~10 nm. The above observation clearly indicates that the 2D CB nanostructure is not indicative of the stacking of rods in the third dimension. Instead, there is a strong possibility that the domain formation happens in the third dimension as well.

4.3.5 Clarification of CB-like appearance in 3D

It is reported by Ni and Khachaturyan (2009) [11] that CB is a 2D nanostructure, in which two interfaces of the nanorods are 220 and $2\bar{2}0$ type and the third interface is 001 type (Figure 4.11(g)). While this proposition is completely acceptable in terms of the topographical arrangements of the nanorods (Figure 4.11(g)), there are two more possibilities; one is with cuboids (Figure 4.5(b)) and another is with irregular octahedron (Figure 4.5(f)) as the basic building blocks.

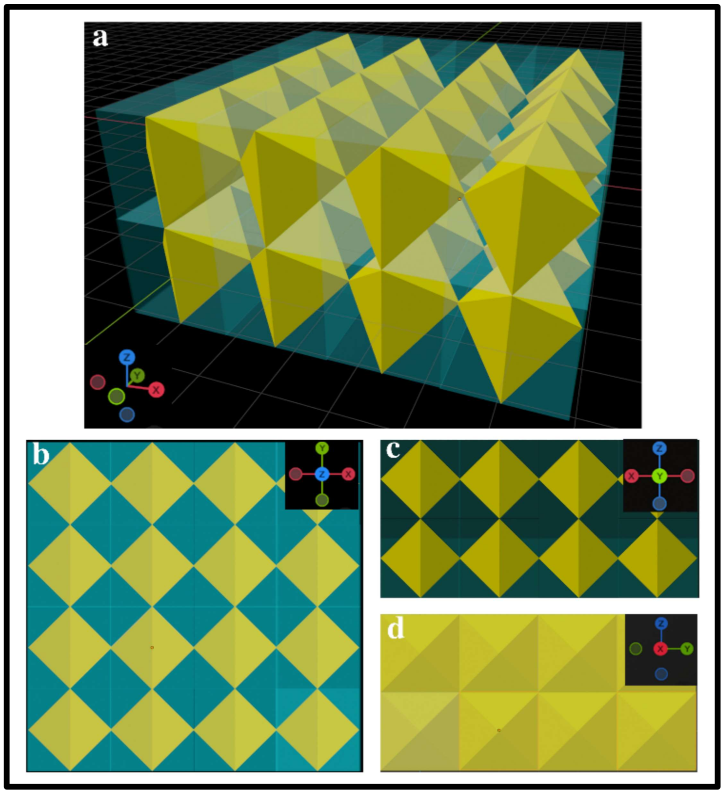

Figure 4.7: *(a) Corner and edge sharing network of irregular octahedra in which the domains in yellow and transparent blue color represent two phase separated domains. The 2D projection of the same network along (b) [001] (c) [010] and (d) [100].*

The cubic lattice as shown in Figure 4.5(c) could be truncated along its four 220 planes to produce a tetragonal structure (Figure 4.5(d)). This tetragonal structure may act as cuboid building block in which four interfaces would be 220 type and two interfaces would be 001 type. The arrangement of such building blocks is shown schematically in Figure 4.5(b) considering the relative rotation among the building blocks. In the schematic diagram

(Figure 4.5(b)), the cubic variants are shown in green and the tetragonal variants are shown in light brown color. The tetragonal structure may further be truncated as shown in Figure 4.5(e) to produce an irregular octahedral structure having all the same symmetry elements as a cube and all its exposed surfaces are {022}. A corner and edge sharing network of this octahedra would appear as a 2D CB from all <100> type of directions as shown in Figure 4.7. This octahedral shape may be considered as one of the phase separated domains (yellow in Figure 4.7(a)) and the remaining space as another phase separated domain (transparent blue in Figure 4.7(a)). Such composition modulation in 3D that gives birth to the CB nanostructure when viewed along <001> directions is further explained in the Figure 4.7(b-d). The projected views along [001] (Figure 4.7(b)), [010] (Figure 4.7(c)) and [100] (Figure 4.7(d)) show perfect CB microstructure. The relative rotation may also be introduced between the octahedral building blocks. However, for the sake of simplicity it has not been introduced. It clearly shows that there are two possible models for the development of CB nanostructure, one leading to a 2D CB and another leading to a 3D CB nanostructure. One has its elementary building block as a nanorod while the other has an irregular octahedra/cuboid as its elementary building block. Stacking of rods as proposed by Ni and Khachaturyan (2009) [11] may also be ruled out due to the observation of subdomains within the rods while tilting in the microscope (Figure 4.6(d)). The issue can be resolved with further confirmatory evidence with APT.

4.3.6 Reconstruction of 3D microstructure via correlative microscopy

Three-dimensional elemental distribution map of Fe, Co, Mn and O as obtained using APT from an analyzed volume of 64 × 64 × 1120 nm^3 (Figure 4.8) shows a uniform distribution of Co and O. However, Fe and Mn are non-uniformly distributed and are partitioned into domains. Based on the enrichment of at least one of the alloying elements, the different domains can be delineated using appropriate threshold concentration values viz. Fe 24 at.% and Mn 29 at.% to develop isoconcentration surfaces as shown in Figure 4.9 (a,b). At the apex region of the tip, Fe and Mn enriched domains are large (~70 nm), whereas in the middle of the tip it appears like a 2D CB and towards the base of the tip once again the domains are large (~70 nm) and the boundary between the domains is jagged. Even within the CB nanostructure in the middle of the tip, there is a variation in size of the domains. Towards the extreme left of the CB domains, the size of the domains is ~10-15 nm, towards the right of it, the size increases to ~20 nm and towards the apex region of the CB domain, it is ~15 nm. Hence, it is not only the chemical segregation, but the variation in size of the segregated domains also points towards an underlying coalescence and growth process of the compositionally separated domains.

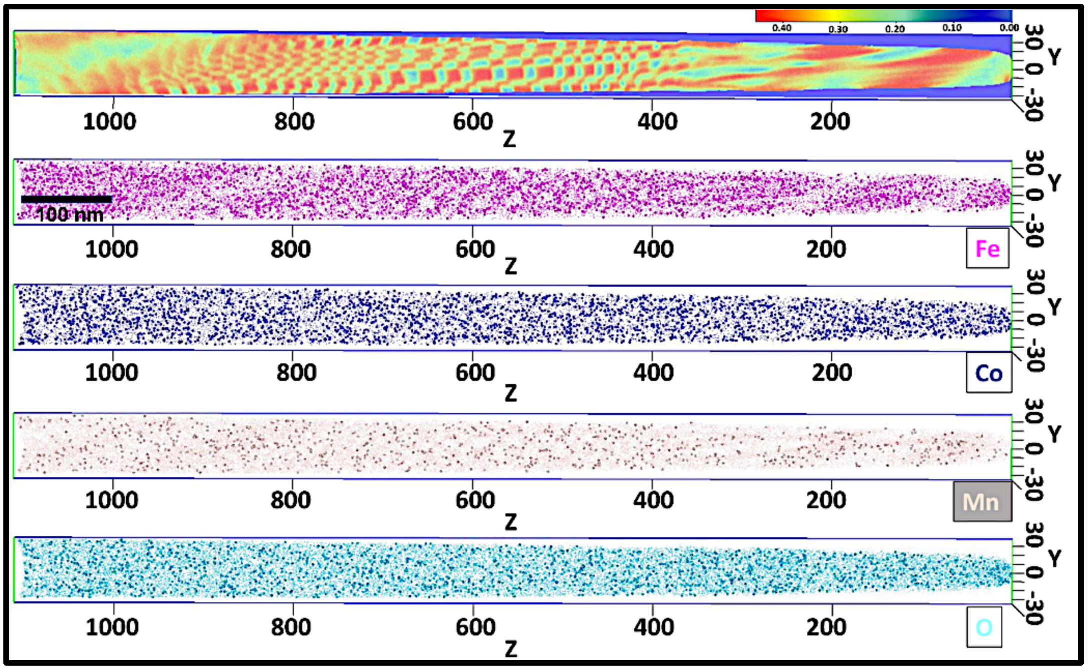

Figure 4.8: *Three-dimensional elemental distribution map of Fe, Co, Mn and O obtained using APT from an analyzed volume of* $64 \times 64 \times 1120$ *nm*^{3} *and contour plot corresponding to Fe 24 at.% and Mn 29 at.% iso-concentration surface (top image). It shows a uniform distribution of Co and O with partitioning of Fe and Mn.*

To clearly differentiate the regions and estimate the local composition, one dimensional concentration depth profile taken along a 10 nm diameter cylindrical region (cyan color inset) of interest has been plotted from the CB region (Figure 4.9(c)). It clearly indicates that Fe and Mn are alternately enriched over every ~10-20 nm length of the cylinder corroborating the presence of alternative Fe and Mn rich nano-domains. This enrichment is accompanied by a minor anti-correlated fluctuation between Co and O. However, the concentrations of Co and O over two consecutive domains are different; this was not so apparent in the STEM-EDS composition maps.

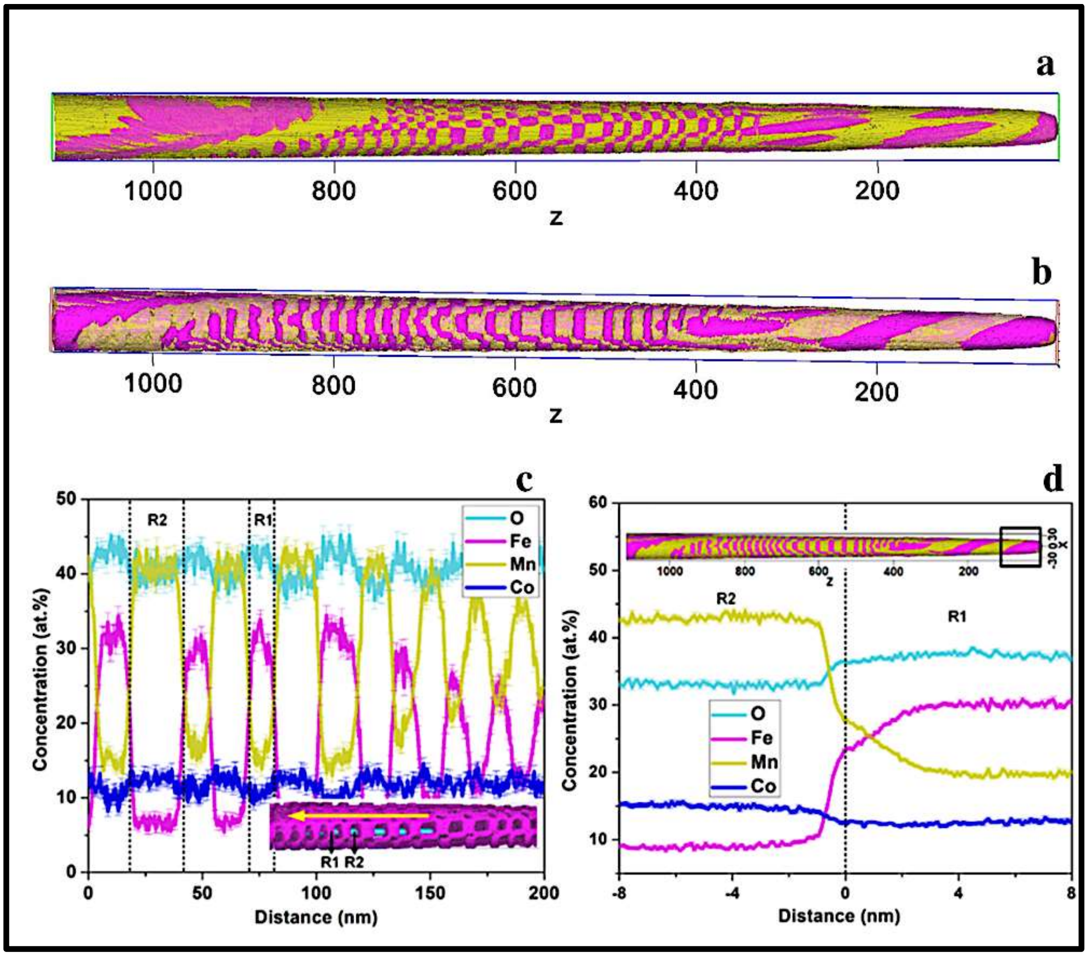

Figure 4.9: *(a), (b) Three-dimensional elemental map of Fe and Mn represented by their respective iso-concentration surfaces in two different orientations. (c) 1D composition depth profile of Fe, Mn, Co and O from the middle of the tip shown in the inset along the direction of the arrow. (d) Proximity histogram corresponding to Fe 24 at.% and Mn 29 at.% iso-concentration surface from the interface marked in square box.*

More importantly, within a particular domain, which is either Fe-rich or Mn-rich, composition fluctuations over a very fine length scale within the domain itself could be observed, as was observed in the TEM dark-field image in Figure 4.6(a) and the corresponding map in Figure 4.6(c). Such composition fluctuations further reinforce the idea of a pseudo-spinodal decomposition of Fe and Mn within the domains themselves. A proximity histogram using Fe isoconcentration surface (marked by square box at the apex of the tip) (Figure 4.9(d)) shows significant enrichment of Fe and O at the core of the partitioned Fe domain similar to that of the Mn enrichment on the adjacent domain (Figure

4.9(d)). The composition profile from the interface of the separated domains indicates that composition fluctuation at the interface is diffuse and that it takes place over a length of ~4 nm. These composition profiles enable us to conclude that similar pseudo-spinodal decomposition takes place throughout the tip. However, it is the kinetics of composition separation and the coalescence of domains which leads to either a 3D CB nanostructure that we have seen here or a 2D CB nanostructure, which others have interpreted as stacking of rods [14].

In order to understand the compositional evolution within the domains, a 24 at.% isoconcentration surface map of Fe (Figure 4.10(a)), an enlarged version of the CB area (Figure 4.10(b)) and a further magnified version of subdomains within a single domain (Figure 4.10(d)) all show that composition fluctuation happens within the Fe-rich CB domain over a length scale of ~1-2 nm (marked by green dotted rectangle in Figure 4.10(d)), which is apparent as fluctuations in the composition profile of Fe (Figure 4.10(c), Figure 4.10(e) and Figure 4.10(f)). Similar fluctuations are also observed for other elements in the same 1D composition profile (Figure 4.10(c)) as marked by the blue dotted rectangle (Figure 4.10(d)). It is expected that equivalent subdomain formation proceeds in the Mn domains also. Isoconcentration surface map of Fe (Figure 4.11(a)), and its 180° rotated view (Figure 4.11(b)) highlights three regions: (i) rod morphology (~70 nm width) with linear interface between separated domains at the apex region of the tip (ii) rod-like morphology (~12 nm width) at the middle region of the tip (iii) rod-like morphology (~ 70 nm width) with a zigzag interface at the bottom part of the tip. The interface of the ~70 nm wide rod at the apex of the tip, which is smooth in Figure 4.11(a) becomes zigzag at a differently rotated view of the same tip in Figure 4.11(d). Similar zigzag interface morphology for the ~70 nm wide rod at the base of the tip is observed in Figures 4.11(c) and 4.11(e).

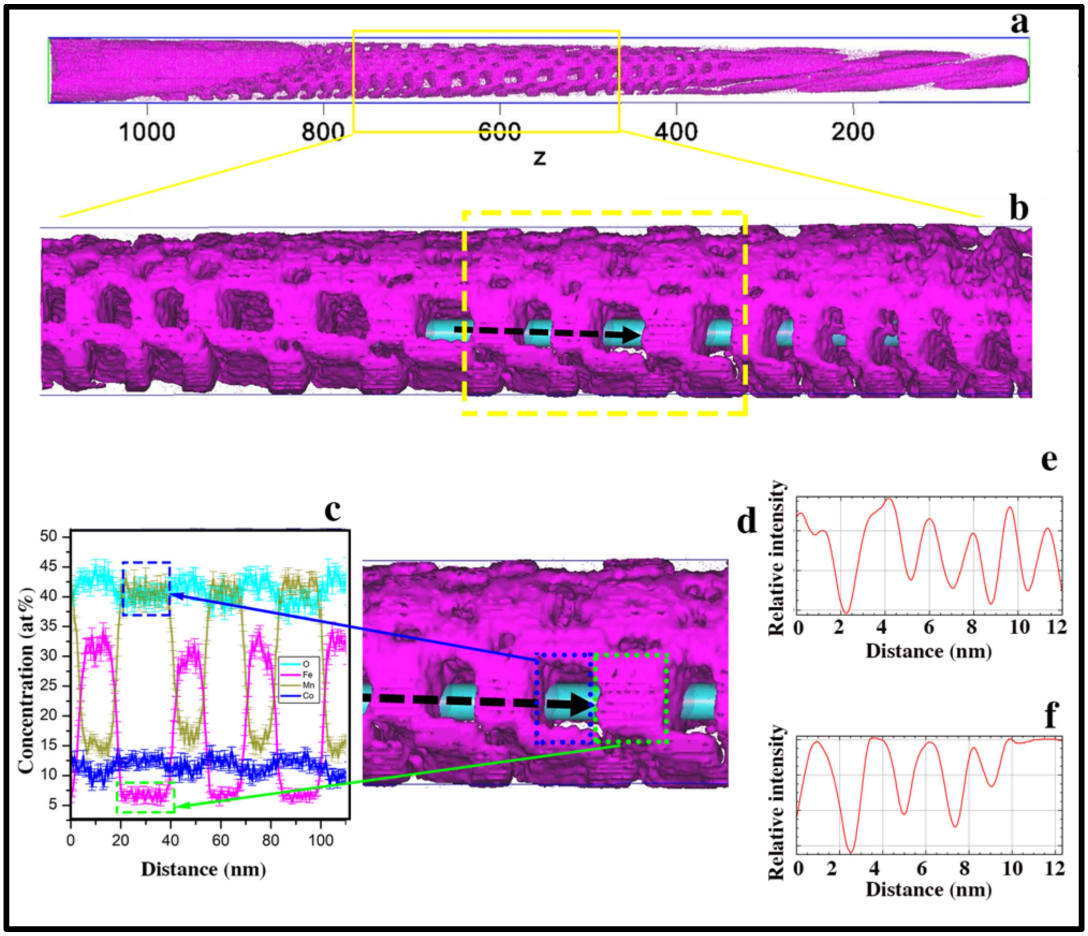

Figure 4.10: *(a) Fe 24 at. % iso-concentration surface, (b) enlarged view of 10 nm cylindrical region of interest in (a) from the middle of the APT tip, (d) magnified version of single Fe-rich domain, (c) 1D composition depth profile of Fe, Mn, Co and O from (d). Intensity variation along (e) x-direction and (f) y-direction of the nanodomains within the plane of the page as observed within the green box in (d).*

In the zigzag interface, any two consecutive compositionally separated surfaces are almost aligned at 90° to one another. This is consistent with the alternate Fe-rich cubic and Mn-rich tetragonal domains along 220 interface observed in Figure 4.3(a). This also points to the coalescence of either the Fe-rich cubic or Mn-rich tetragonal domains along 040 or 004 directions (Figure 4.3(a)). This is also schematically presented in Figure 4.11(h). When they coalesce along 040 or 004 directions they essentially become a rod in projected view (guided by cyan and red dotted line in Figure 4.11(h)), as observed in the TEM images and schematically presented in Figure 4.11(g). Due to the coalescence along 040/004 direction it is inclined at ~45° with respect to the parental domain.

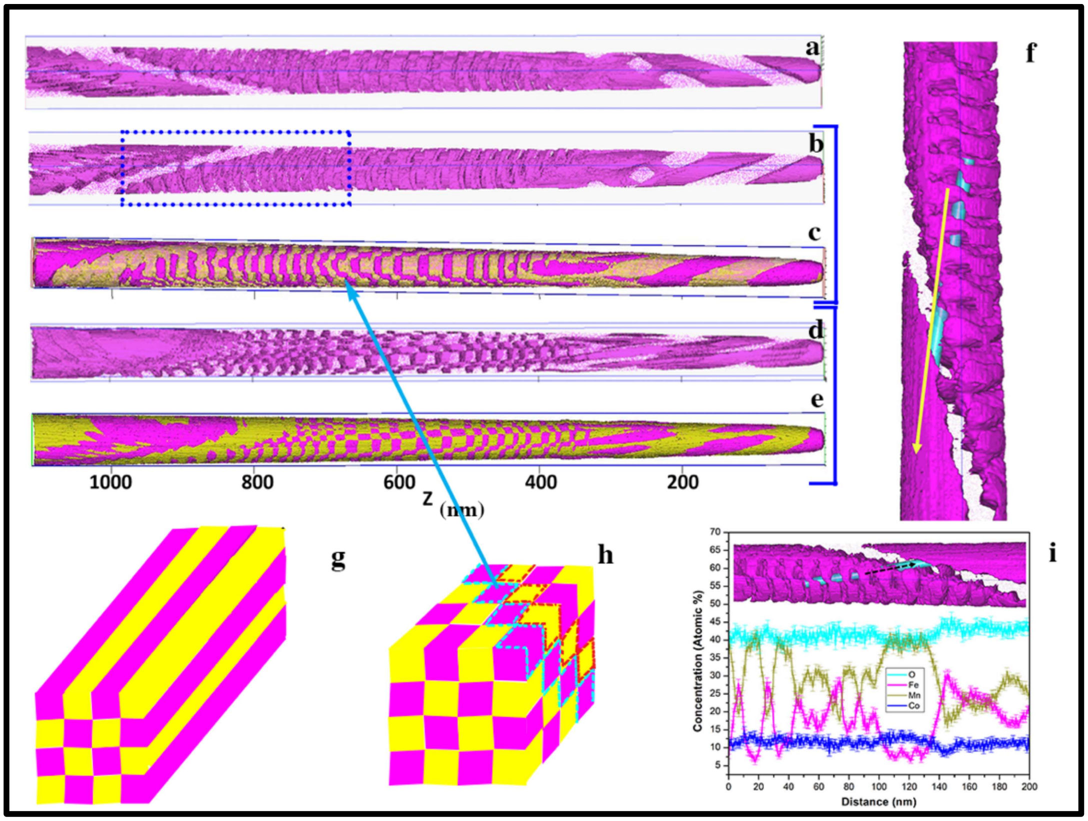

Figure 4.11: *(a) and (b) Two different (180° rotated) orientations of Fe 24 at.% iso-concentration surface (c) Fe 24 at.% and Mn 29 at.% iso-concentration surface, (d) Fe 24 at.% iso-concentration surface showing the CB nanostructure at the middle, (e) Fe and Mn iso-concentration surface showing the CB nanostructure at the middle of the APT tip, (f) 10 nm cylindrical region (cyan colour rod) of interest of Fe iso-concentration surface in (b), (g), (h): schematic representations of 2D and 3D nanostructured CB, respectively, (i) 1D composition profile of Fe, Mn, Co, O along the arrow in (f).*

In the Fe and Mn isoconcentration surface image (Figure 4.11(c)), the small cuboids at the centre of the tip are also seen to coalesce along the 004 or 040 direction and they appear to be curved as they are represented in Figure 4.11(h). The 1D composition profile taken along the 10 nm cylindrical region of interest (Figure 4.11(f)) is as shown in Figure 4.11(i). It indicates that there is not only the difference in size of the domains that exists, but that it is also accompanied with a composition variation. In the CB domain and in the partially coalesced rod domain the composition of Fe and Mn are similar, with a signature of secondary spinodal in them. However, on both sides of them the composition is different.

4.4 Conclusions

Combined TEM and APT study indicates that CB evolution is a hopping process of the material in its energy landscape from one local minimum to another local minimum. Here, we have clearly shown that the earlier report by Ni and Khachaturyan (2009) [14] is only partially complete. The cross-twinning, that initially defines the CB morphology, occurs in order to reduce the strain in the lattice. Further compositional segregation and solid body rotation help to reduce the interfacial strain. Recurring pseudo-spinodal decomposition within the initial domains leads to a finer-well-organized subdomains within the CB. Further attempts to reduce the interfacial strain lead to the coalescence of the nanodomains, which then appear as rods in a 2D projection. Rods with larger dimensions are grown by the coalescence of smaller domains. The kinetics of all these processes are extremely important in predictive design of the nanostructure either in 2D or in 3D. In addition, two different phase that can have magnetic states, could be suitably tailored to design its functionality or differential flux permeability that this material is poised to exhibit. The concept of CB nanostructure evolution presented in this chapter could also be extended to other materials.

References

[1] H.F. Hamann, M. O'Boyle, Y.C. Martin, M. Rooks, H.K. Wickramasinghe, Ultra-high-density phase-change storage and memory, Nat. Mater. 5 (2006) 383–387. https://doi.org/10.1038/nmat1627.

[2] S. Parkin, S.H. Yang, Memory on the racetrack, Nat. Nanotechnol. 10 (2015) 195–198. https://doi.org/10.1038/nnano.2015.41.

[3] S.N. Piramanayagam, Perpendicular recording media for hard disk drives, J. Appl. Phys. 102 (2007) 011301. https://doi.org/10.1063/1.2750414.

[4] D. Wiesmann, C. Rawlings, R. Vecchione, F. Porro, B. Gotsmann, A. Knoll, D. Pires, U. Duerig, Multi Tbit/in^2 storage densities with thermomechanical probes, Nano Lett. 9 (2009) 3171–3176. https://doi.org/10.1021/nl9013666.

[5] K.S. Leschkies, R. Divakar, J. Basu, E. Enache-Pommer, J.E. Boercker, C.B. Carter, U.R. Kortshagen, D.J. Norris, E.S. Aydil, Photosensitization of ZnO nanowires with CdSe quantum dots for photovoltaic devices, Nano Lett. 7 (2007) 1793–1798. https://doi.org/10.1021/nl070430o.

[6] R. Garcia, A.W. Knoll, E. Riedo, Advanced scanning probe lithography, Nat. Nanotechnol. 9 (2014) 577–587. https://doi.org/10.1038/nnano.2014.157.

[7] J. Basu, C.B. Carter, R. Divakar, B. Mukherjee, N. Ravishankar, Nanopatterning by solid-state dewetting on reconstructed ceramic surfaces, Appl. Phys. Lett. 94 (2009) 2009–2011. https://doi.org/10.1063/1.3127442.

[8] J. Basu, C. Barry Carter, R. Divakar, V.B. Shenoy, N. Ravishankar, Modified electron-beam-induced deposition of metal nanostructure arrays using a parallel electron beam, Appl. Phys. Lett. 93 (2008) 133104. https://doi.org/10.1063/1.2992193.

[9] S. Park, Y. Horibe, T. Asada, L.S. Wielunski, N. Lee, P.L. Bonanno, S.M. O'Malley, A.A. Sirenko, A. Kazimirov, M. Tanimura, T. Gustafsson, S.-W. Cheong, Highly aligned epitaxial nanorods with a checkerboard pattern in oxide films, Nano Lett. 8 (2008) 720–724. https://doi.org/10.1021/nl072848s.

[10] C. Leroux, A. Loiseau, D. Broddin, G. Vantendeloo, Electron microscopy study of the coherent two-phase mixtures $L1_0 + L1_2$, in Co–Pt alloys, Philos. Mag. B. 64 (1991) 57–82. https://doi.org/10.1080/13642819108207603.

[11] Y. Ni, A.G. Khachaturyan, From chessboard tweed to chessboard nanowire structure during pseudospinodal decomposition, Nat. Mater. 8 (2009) 410–414.

https://doi.org/10.1038/nmat2431.

[12] B.S. Guiton, P.K. Davies, Nano-chessboard superlattices formed by spontaneous phase separation in oxides, Nat. Mater. 6 (2007) 586–591. https://doi.org/10.1038/nmat1953.

[13] A.M. Abakumov, R. Erni, A.A. Tsirlin, M.D. Rossell, D. Batuk, G. Nénert, G. Van Tendeloo, Frustrated octahedral tilting distortion in the incommensurately modulated $Li_{3x}Nd_{2/3-x}TiO_3$ perovskites, Chem. Mater. 25 (2013) 2670–2683. https://doi.org/10.1021/cm4012052.

[14] Y. Ni, A.G. Khachaturyan, Mechanism and conditions of the chessboard structure formation, 56 (2008) 4498–4509. https://doi.org/10.1016/j.actamat.2008.05.035.

[15] K.-I. Udoh, A.M. El Araby, Y. Tanaka, K. Hisatsune, K. Yasuda, G. Van Tendeloo, J. Van Landuyt, Structural aspects of AuCu I or AuCu II and a cuboidal block configuration of f.c.c. disordered phase in AuCu-Pt and AuCu-Ag pseudobinary alloys, Mater. Sci. Eng. A. 203 (1995) 154–164. https://doi.org/10.1016/0921-5093(95)09850-X.

[16] G. van Tendeloo, S. Amelinckx, Long-period antiphase boundary structures in the ordered alloy Au4Zn. I. one-dimensional long-period antiphase boundary structure, Phys. Status Solidi. 43 (1977) 553–564. https://doi.org/10.1002/pssa.2210430224.

[17] H. Zheng, J. Kreisel, Y. Chu, R. Ramesh, L. Salamanca-Riba, Heteroepitaxially enhanced magnetic anisotropy in $BaTiO_3$–$CoFe_2O_4$ nanostructures, Appl. Phys. Lett. 90 (2007) 113113. https://doi.org/10.1063/1.2713131.

[18] C.L. Zhang, C.M. Tseng, C.H. Chen, S. Yeo, Y.J. Choi, S.W. Cheong, Magnetic nanocheckerboards with tunable sizes in the Mn-doped $CoFe_2O_4$ spinel, Appl. Phys. Lett. 91 (2007) 233110. https://doi.org/10.1063/1.2821838.

[19] C.L. Zhang, S. Yeo, Y. Horibe, Y.J. Choi, S. Guha, M. Croft, S.-W. Cheong, S. Mori, Coercivity and nanostructure in magnetic spinel $Mg(Mn,Fe)_2O_4$, Appl. Phys. Lett. 90 (2007) 133123. https://doi.org/10.1063/1.2717568.

[20] P.M. Woodward, A chessboard at the nanoscale, Nat. Mater. 6 (2007) 549–551. https://doi.org/10.1038/nmat1970.

[21] H. Zhang, K.G. Pradeep, S. Mandal, D. Ponge, H. Springer, D. Raabe, Dynamic strain-induced transformation: An atomic scale investigation, Scr. Mater. 109 (2015) 23–27. https://doi.org/10.1016/j.scriptamat.2015.07.010.

[22] I. Basu, K.G. Pradeep, C. Mießen, L.A. Barrales-Mora, T. Al-Samman, The role of atomic scale segregation in designing highly ductile magnesium alloys, Acta Mater.

116 (2016) 77–94. https://doi.org/10.1016/j.actamat.2016.06.024.

[23] J.W. Christian, S. Mahajan, Deformation twinning, Prog. Mater. Sci. 39 (1995) 1–157. https://doi.org/10.1016/0079-6425(94)00007-7.

[24] C. Li, X. Han, F. Cheng, Y. Hu, C. Chen, J. Chen, Phase and composition controllable synthesis of cobalt manganese spinel nanoparticles towards efficient oxygen electrocatalysis, Nat. Commun. 6 (2015) 7345. https://doi.org/10.1038/ncomms8345.